

GPS-Denied Navigation Using Low-Cost Inertial Sensors and Recurrent Neural Networks*

Ahmed AbdulMajuid^{a,*}, Osama Mohamady^a, Mohannad Draz^a, Gamal El-bayoumi^a

^a*Aerospace Engineering Department, Cairo University, ElGamaa St., Giza 12613, Egypt*

Abstract

Autonomous missions of drones require continuous and reliable estimates for the drone's attitude, velocity, and position. Traditionally, these states are estimated by applying Extended Kalman Filter (EKF) to Accelerometer, Gyroscope, Barometer, Magnetometer, and GPS measurements. When the GPS signal is lost, position and velocity estimates deteriorate quickly, especially when using low-cost inertial sensors. This paper proposes an estimation method that uses a Recurrent Neural Network (RNN) to allow reliable estimation of a drone's position and velocity in the absence of GPS signal. The RNN is trained on a public dataset collected using Pixhawk. This low-cost commercial autopilot logs the raw sensor measurements (network inputs) and corresponding EKF estimates (ground truth outputs). The dataset is comprised of 548 different flight logs with flight durations ranging from 4 to 32 minutes. For training, 465 flights are used, totaling 45 hours. The remaining 83 flights totaling 8 hours are held out for validation. Error in a single flight is taken to be the *maximum* absolute difference in 3D position (MPE) between the RNN predictions (without GPS) and the ground truth (EKF with GPS). On the validation set, the median MPE is 35 meters. MPE values as low as 2.7 meters in a 5-minutes flight could be achieved using the proposed method. The MPE in 90% of the validation flights is bounded below 166 meters. The network was experimentally tested and worked in real-time.

Keywords: GPS-Denied Environment, Recurrent Neural Network, Inertial Navigation, UAV Sensor Fusion

1. Introduction

Many applications require accurate positioning in the absence of GPS. Examples include indoor navigation performed by robots in warehouses or garages, underwater operations performed by Autonomous Under Water Vehicles (AUVs), and self-driving cars or drones moving in tunnels, under bridges, or in dense urban environments.

Many approaches were taken to solve the navigation problem in GPS-denied environments. In robotics and self-driving cars, it is common to assist the inertial sensors with cameras [1], laser scanners [2], radar [3], or car On-Board Diagnostics (OBD) [4]. However, aside from the added cost, these sensors impose constraints on the environment or vehicle operation to function properly.

Before GPS, the classical aerospace positioning method was the Inertial Navigation System (INS). INS utilizes thoroughly calibrated high-grade inertial sensors and complex navigation algorithms to estimate the position from acceleration and angular rates [5]. However, the cost of

such an approach is not justifiable in a commercial context.

A newer trend is to use Artificial Intelligence (AI) methods to assist the INS. These methods can both reduce the need for costly calibration [6] and allow the use of lower-cost inertial sensors [7].

Different AI algorithms can be utilized in various steps in the inertial navigation process. One popular algorithm is Radial Basis Function Neural Network (RBFNN), which was used to predict the errors in position and velocity estimated by the INS given a window of estimates [8] or Accelerometer measurements [9]. It can also be used along with an EKF to estimate position and attitude from the Accelerometer, Gyroscope (collectively Inertial Measurement Unit IMU), and Magnetometer measurements [10].

Variations of Multi-Layer Perceptrons (MLP) are also commonly used. MLPs were used to predict position increments from velocity and heading [11], and predict the errors in heading and velocity given their changes from one time step to another [12]. They were also used to predict the changes in latitude and longitude given the IMU measurements and INS velocity [13].

Recently, Recurrent Neural Networks (RNN) are being utilized for their superiority with time series problems. RNNs were trained to predict the INS position and velocity errors using the INS change in velocity and heading as input [14]. Long Short-Term Memory (LSTM) net-

*©2021. This manuscript version is made available under the CC-BY-NC-ND 4.0 license <https://creativecommons.org/licenses/by-nc-nd/4.0/>

*Corresponding author

Email addresses: amajuid@hotmail.com (Ahmed AbdulMajuid), o.mohamady@eng.cu.edu.eg (Osama Mohamady), m_draz@cu.edu.eg (Mohannad Draz), gelbayoumi@cu.edu.eg (Gamal El-bayoumi)

works, which are enhanced RNNs, can also use the history of Kalman gain from the Kalman Filter to predict the INS velocity and position errors [15].

Other methods like Input-Delay Neural Networks (IDNN) [16], Ensemble Learning [17], Nonlinear Autoregressive with exogenous input (NARX) [18, 19], and Fuzzy Inference Systems (FIS) [20] are also applied with promising results.

Contributions in this Paper

- None of the work pointed above used an aerial vehicle as a host; using an aerial vehicle introduces more vector components in position, velocity, and attitude. Aerial vehicles are also capable of performing more complex maneuvers than cars or boats.
- Most of the previous work used relatively high-grade sensors (cost 2000\$ to 9000\$), which are easier to model. This paper utilizes extremely low-cost sensors (< 50\$). Low-cost sensors usually have more sources of errors and exhibit non-consistent error behaviors.
- The experiments carried in earlier work use the same hardware to collect both training and validation data. That is, a single sensor is used to collect data in a single long trip using the same host vehicle. The work presented in this paper uses data collected from many different sensors and host vehicles under different conditions. The error characteristics of each sensor unit differ from the others even if all these units are of the same sensor model.

2. Pixhawk and PX4 Drone Flight Stack

The Pixhawk is a commercial low-cost (about \$170) flight controller board suitable for research and industrial applications. It integrates an ARM processor, IMU, Barometer, Magnetometer, and additional components required for flight monitoring and control [21]. It also accepts a micro SD card, on which it saves the flight data, including raw sensor measurements, control actions, hardware status, and other important information. The community that developed the first Pixhawk is PX4; they maintain a fully functional and open source autopilot software called PX4 autopilot [22]. In addition to the low-level sensor drivers, control loops, and planning algorithm, PX4 autopilot features an INS/GPS integration routine, called EKF2 [23], as a part of its Estimation and Control Library (ECL) [24]. EKF2 fuses measurements from IMU, Barometer, Magnetometer, and GPS to estimate the drone’s states, namely, attitude represented in quaternions, velocity, and position in local frame (North-East-Down). EKF2 estimates, too, are logged on the SD card.

The PX4 team maintains a database of flight logs [25], where users worldwide upload actual flight data collected from real flights. The database contains thousands of logs

collected using different Pixhawk versions and using various host vehicles. The data used in this work are downloaded from the PX4 database, no simulated data is used. Only flight logs for Pixhawk4 [26] - the most recent Pixhawk version - were downloaded. Figure 1 shows the Pixhawk4 board and the standard M8N GPS used with it. Sensors models used in the Pixhawk4 board are listed in Table 1.



Figure 1: Pixhawk4 autopilot hardware with a Neo M8N GPS Module connected

Table 1: Pixhawk4 sensors

Sensor	Model	Price
IMU	ICM-20689 [27] & BMI055 [28]	\$3
Magnetometer	IST8310 [29]	\$3
Barometer	MS5611 [30]	\$10

The logs downloaded from the PX4 database contain the raw sensor measurements (IMU, Barometer, and Magnetometer); those are treated as network inputs (features). The logs also contain the flight states estimated by the EKF2 (attitude, velocity, and position); those are treated as network outputs (labels). Other hardware health data are also logged, and those are used to remove the corrupted logs.

Flights used for this work ranged from 4 to 32 minutes, with an average flight duration of 6 minutes. A total of 548 flights are used, with a combined duration of about 54 hours. Only 465 flights are used for training (about 45 hours), and the remaining 83 flights (about 8 hours) are held for validation.

The logs are collected using different types of host vehicles, although mostly Quadcopters, some Fixed Wing (FW) and Vertical Takeoff and Landing (VTOL) vehicles were used. Figure 2 summarizes different vehicle types found on the database and used for this work. The most

popular vehicles found in the PX4 logs database are DJI Flamewheel F450 and Holybro S500, shown in Table 2

Table 2: Different host vehicle types

Vehicle Type	Number of Logs
Quadrotor	526
Fixed Wing	19
Standard VTOL	8
Octorotor	4
Tiltrotor VTOL	2
Hexarotor	1



Figure 2: DJI Flamewheel F450 (left) and Holybro S500

3. PX4’s Extended Kalman Filter Algorithm (EKF2)

The PX4’s EKF2 algorithm consists of two steps; prediction, using the IMU and inertial navigation techniques, and correction using any other available sensors. In the prediction step, the angular rates $\omega_x, \omega_y, \omega_z$ measured by the Gyroscope in the vehicle’s body frame and the accelerations a_x, a_y, a_z measured by the Accelerometer in the same frame are integrated numerically to obtain delta angles and delta velocities. Then, bias terms are subtracted, these terms represent all of the inertial navigation error sources, and as a part of the EKF state vector, they are updated with each iteration.

The debiased delta angles are then corrected for the earth’s rotation rate effect, which is a function of the latitude; this can be taken as the home latitude. The corrected delta angles are transformed to delta quaternions and those are used with the previous quaternions to calculate the vehicle’s new attitude in quaternions q_1, q_2, q_3, q_4 . This process is outlined in Figure 3.

This new attitude is then used to transform the debiased delta velocities from the body frame to the local frame. Then the gravity effect is added, which is also dependent on the latitude. The resulting corrected delta velocity is added to the previous velocity to obtain the new velocity in the local frame V_N, V_E, V_D . Which is integrated again to obtain the position increments, those are added to the previous position to obtain the new position in the local frame P_N, P_E, P_D . This process is outlined in Figure 4.

These predictions diverge quickly from the actual state values because numerical integration is applied thrice, and

the biases used for compensation are not perfectly accurate [31]. Biases even vary with time, so they need to be updated regularly. These problems have more significant effects when low-cost sensors are used because their errors are not consistent and hard to model [32], which is the case with commercial autopilots like the Pixhawk. Figure 5 shows the predictions of the PX4 EKF2 in a real flight when GPS is not used to correct the IMU predictions.

The second step in EKF2 is the correction. Whenever measurements from another sensor are available, the predictions from the first step are corrected. The Barometer is used to correct the down component of the position, while GPS corrects the other two components of position and the three velocity components. The Magnetometer helps to correct the attitude. Figure 6 shows the outline of the EKF prediction-correction architecture.

Sensors other than the IMU are also used to correct the IMU biases in the correction step to allow for better IMU predictions in the next timestep. IMU bias correction is accomplished by adding the biases in delta angles and delta velocities to the EKF state vector.

4. Proposed System

This paper proposes a new method to predict the states from the IMU measurements without a need for GPS correction, sensor calibration, or navigation equations. The main idea is to replace the processes shown in Figure 3 and Figure 4 with a Neural Network NN, Figure 7. The network is basically learning the sensors’ error models, measurement rotation, and integration.

The NN in this context can be viewed as a complex curve fitting function. In curve fitting, a function, polynomial for example, is established to represent the relation between an independent variable, like time, and a dependent variable, like the price of an item. The coefficients of this polynomial are calculated from a collection of input-output pairs, that is, a table of time and price points (training set). Once the polynomial coefficients are calculated, new values of time can be substituted into the polynomial to predict the price, for example, in the future. New inputs with known outputs are then given to the computed fitting function to test its validity. This test examines the accuracy on data not seen previously during fitting (validation set). NNs follow the same concept but can fit more complex relations using combinations of non-linear functions and a large number of parameters, called weights. In this case, the independent variables (NN inputs) are the IMU, Barometer, and Magnetometer measurements. The dependent variables (NN outputs) are the changes in position and velocity.

The network architecture shown in Figure 7 is called dense architecture. A better alternative when inputs or outputs are in data series form is the Recurrent Neural Network (RNN). RNNs are better suited for series of arbitrary lengths and are popular with speech recognition

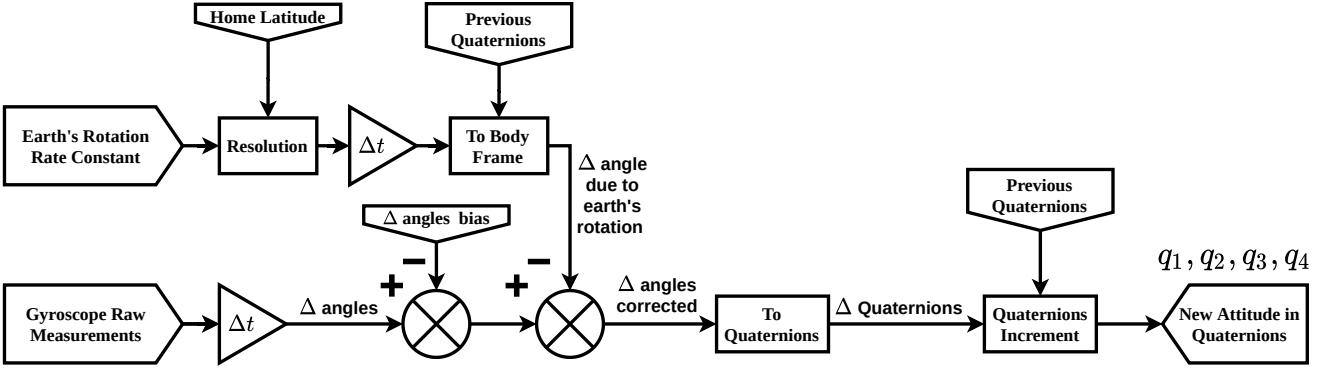


Figure 3: Attitude prediction from Gyroscope measurements in the EKF2 prediction step

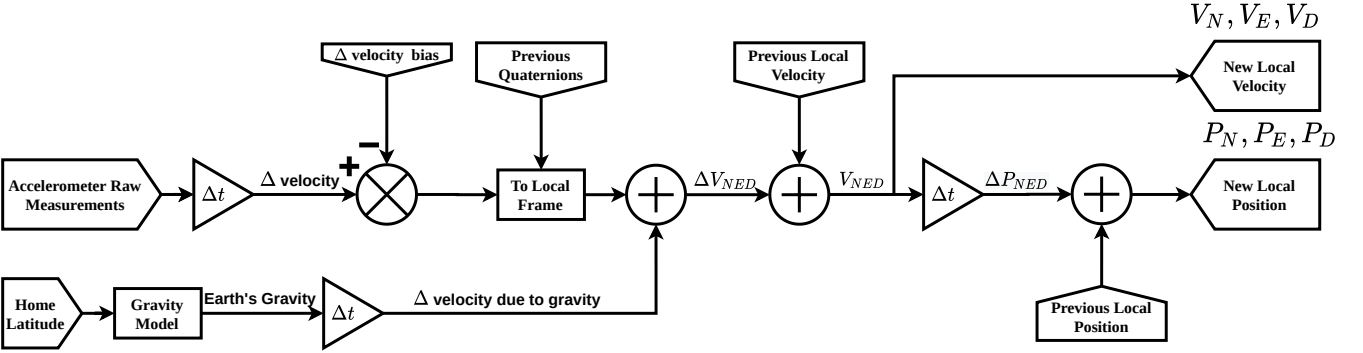


Figure 4: Velocity and position prediction from attitude and Accelerometer measurements in the EKF2 prediction step

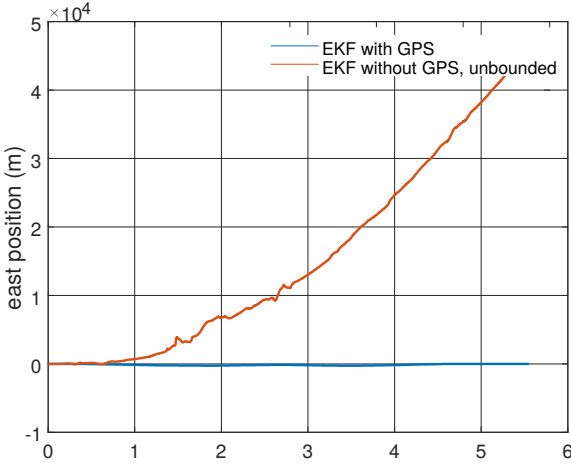


Figure 5: EKF2 east position predictions when no GPS aiding is used

and time series forecasting applications. RNNs pass memory information from earlier points in the sequence to later points and use them for later predictions. The architecture used in this paper is composed of recurrent layers followed by a single dense layer.

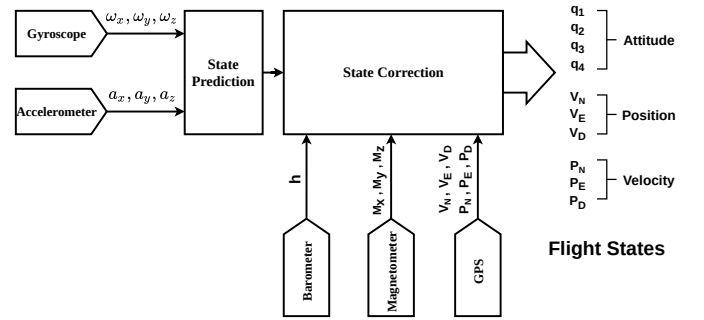


Figure 6: EKF Prediction-Correction Architecture

5. Data Preprocessing

No filtration is applied to the raw sensor measurements given to the network. All the preprocessing steps mentioned here are used to control the input rates, remove corrupted data from the training set, or divide the inputs into segments.

5.1. Different Update Rates of Different logged messages

In the flight log file created by the PX4 stack, different sensor data are stored in different messages. The frequency of the logged data is not the same in all messages; different frequencies are shown in Table 3. This means that

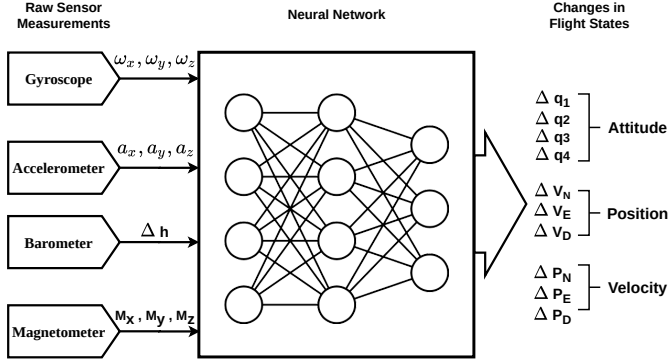


Figure 7: Proposed NN-Based Estimator

between two consecutive outputs expected from the network, several inputs arrive. Furthermore, the input size differs from one step to another; for example, only the IMU measurements are available at one step, but in the next step, only Barometer data might be available, and so on. To solve this problem, sensor data are averaged between each two consecutive logged EKF outputs (Figure 8). This averaging unifies the input and output frequency to 5 Hz.

Table 3: Different sensors rates in the log file

Message	Contents	Update Rate
IMU	Angular Rates $\omega_x, \omega_y, \omega_z$ and Linear Accelerations a_x, a_y, a_z in body frame	84 Hz
Barometer	Temperature T and Altitude h	67 Hz
Magnetometer	Magnetic Field Components M_x, M_y, M_z in body frame	45 Hz
EKF	Estimated states, attitude q_1, q_2, q_3, q_4 , Velocity V_N, V_E, V_D and Position P_N, P_E, P_D in Local Frame	5 Hz

5.2. Data Windowing

RNNs are used with sequences because they learn the dependencies in sequences of data. The length of the sequence fed into the network at a time is called window size. For example, if the network translates a text from one language to another, the window might be one sentence, paragraph, or page. In this problem, the window length is defined by the number of timesteps, knowing that each timestep is 0.2 seconds. Optimal window size depends on the problem and is considered a design parameter and usually selected by trials. Large windows require a longer time for both training and inference, and smaller windows might not capture enough dependencies.

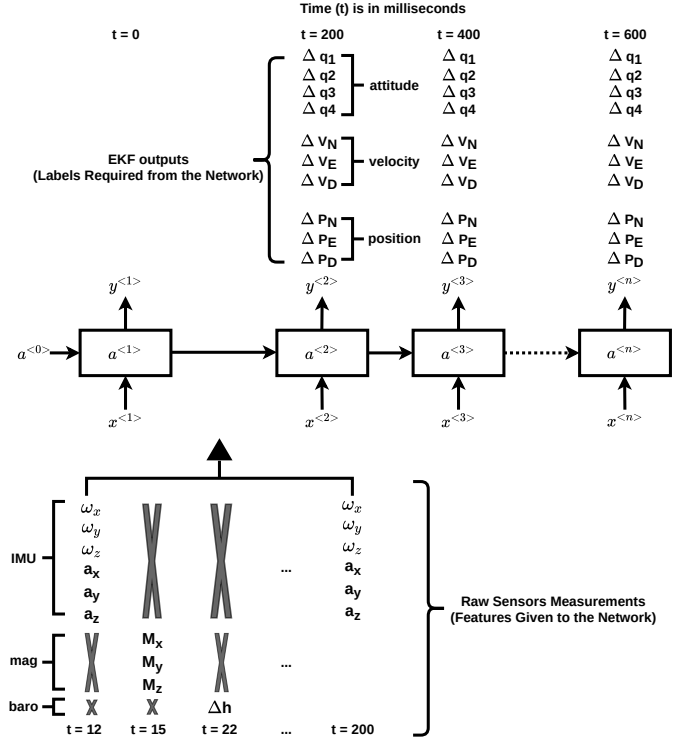


Figure 8: Unifying the different rates of features and labels retrieved from the flight logs

5.3. Differencing

Inertial sensors measure rates, so they can only be used to calculate increments in flight states (position and velocity). Then the absolute values of the states are calculated by accumulating these increments to the initial conditions. This is why it is better to have the network predict increments and accumulate the predictions later. So, in pre-processing, differencing is applied to the labels (position, velocity, and attitude) and to the input Barometer altitude. Differencing is done by subtracting every point in the sequence from the next one.

Another advantage of this approach is that a prediction at a time step is not affected by an erroneous prediction of a previous step; only the reconstructed path is affected. As a result, the errors in the predicted states will be local, and though they cause a constant offset between the true and predicted states for the rest of the flight, this error *does not grow* with time. Figure 9 and Figure 10 show how an erroneous prediction results in a bounded error that does not grow with time. This is only possible because changes in states are being predicted, not the states themselves. The offset grows up when multiple consecutive errors in the same direction are made, and grows down when errors of opposing direction are made.

5.4. Ground Time Trimming

While tuning the network, it was found that the network “leaks”, that is, when the true values are not changing, the

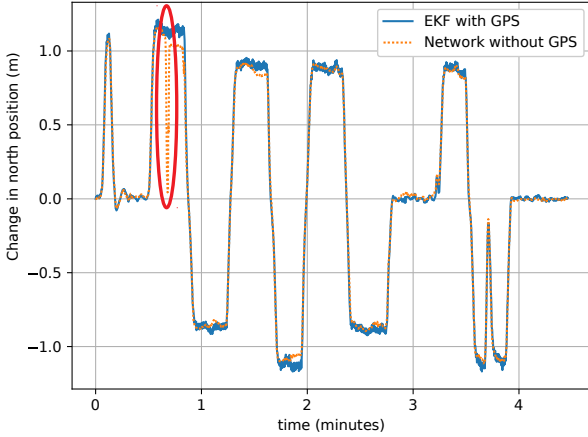


Figure 9: Changes in a state as predicted by the network as opposed to the true changes

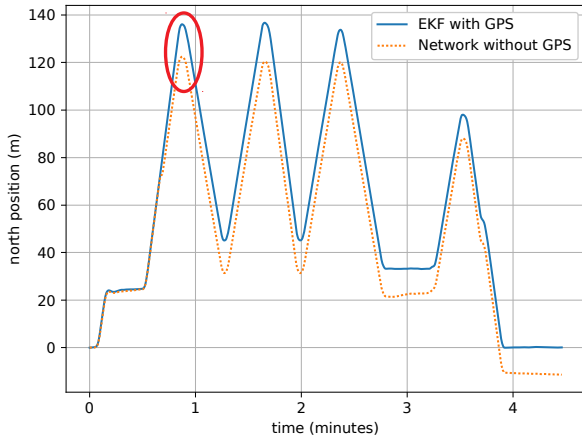


Figure 10: A mispredicted change results in an offset when reconstructing the state path, but it does not grow

network drifts slowly. But when the true values are changing, the network predictions follow the changes correctly. This can be seen in Figure 11. The network learned this behavior from the ground truth values. It turns out that the EKF2 estimates drift when the drone is on the ground, before takeoff and after landing, even if a good GPS signal is available.

Figure 12 is an example of a thirty-minute log of which about ten minutes are erroneous ground truth values. This behavior exists in most flights, so it is difficult for the network not to learn it. This behavior can be corrected by trimming the ground time from the logs before feeding them to the network.

5.5. Manual Dataset Cleanup

Further manual cleanup was applied to remove other problems in the dataset. For example, some logs where

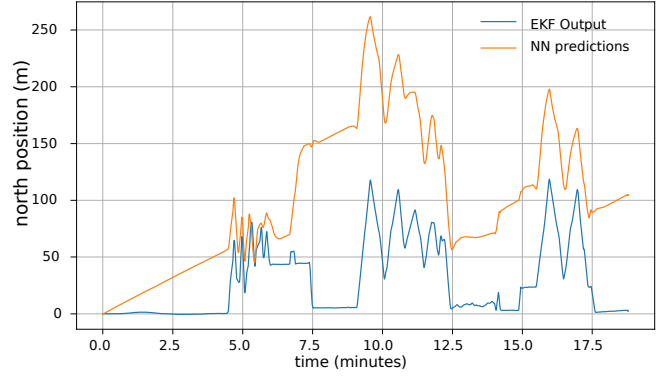


Figure 11: Network predictions drifting when the true values are not changing

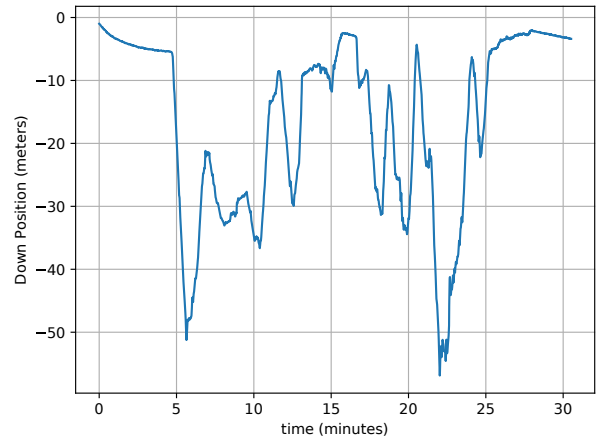


Figure 12: EKF estimates drifting when the drone is on the ground

the drone did not even takeoff might be as long as 20 minutes. Other logs collected with a poorly tuned EKF, or when a hardware fault occurred are also removed. This intensive cleanup reduced the number of logs from 943 to 548. Figure 13 shows a log found in the database with a claimed duration of about 21 minutes. After trimming the ground time it was found that the entire log is corrupted, and no actual takeoff took place.

6. Network Design and Hyperparameters Tuning

Neural Network design is an iterative process. Many design parameters that determine the network shape and characteristics are to be selected. Other design decisions are concerned with how the network is trained, that is, how the weights are updated. These decisions result in the selection of proper *hyperparameters*. This section describes how each design parameter and hyperparameter was selected. Figure 14 shows the general network architecture. The number of layers, their types, and the number of nodes in each layer are some of the design decisions.

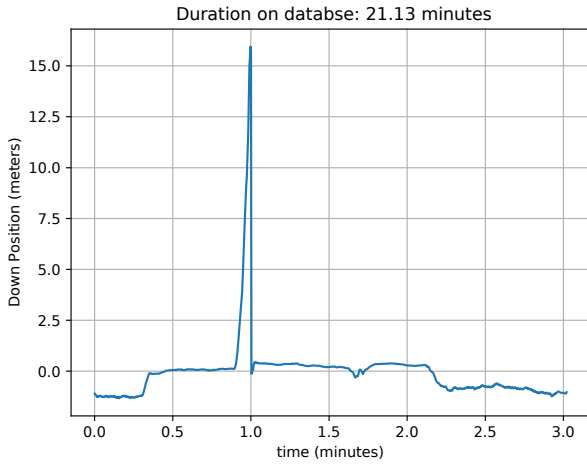


Figure 13: Corrupted log with no actual takeoff

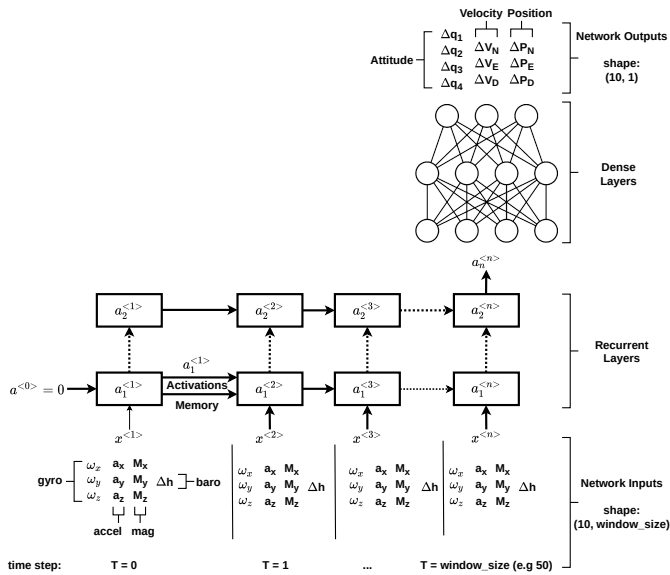


Figure 14: General Network Architecture

To decide on hyperparameters, a performance index is needed, but the system can be assessed from two different perspectives

1. As a neural network

In this case, a good network makes as many correct predictions as possible. Recall that predictions are changes in the states, not the states themselves. Correct prediction means that the predicted value is close enough to the true value because exact correctness is not feasible with floats.

2. As a Navigation System

In this case, a good design results in the smallest difference between the predicted and the true paths. It can also be assessed by the growth of error with time. In this case, the reconstructed states plots are visualized, not the predictions themselves.

If a design makes a single mistake at the beginning of a given flight, a constant offset is kept between the true and estimated path for the entire flight duration. This design is a good NN but is a lousy navigation system. Another design might make multiple mistakes at the end of a flight, so their effect on the path will be negligible. This design is better from a Navigation perspective but is a worse NN.

During training, only the first perspective can be considered through the loss (cost) value. The second assessment method requires post-processing after the network is trained. The 3D path of every validation flight is compared to the true 3D path. The maximum difference for each flight is recorded. The median of these maximum values is calculated and called MPE. The selection of the upcoming hyperparameters was made according to MPE as a single performance index.

6.1. Loss Function

The loss function determines how far the prediction is from the true value, thus, how much the weights need to be changed. Standard loss functions used with timeseries forecasting like Mean Absolute Error (MAE), Mean Square Error (MSE), and Huber Loss did not perform well in this particular problem. This is because the output signals of the network have different orders of magnitude. For example, velocity components are bounded by the vehicle's propulsive and structural capabilities. They are considerably smaller than the position components that can grow as large as the drone's datalink to the ground station can support. This translates to large velocity errors, Figure 15, even when the position errors are small, Figure 16. However, position estimation is more complex than velocity estimation and implicitly utilizes it. This is the result of the network paying more attention to the signals that produce larger error magnitudes, thus have larger contribution to the cost.

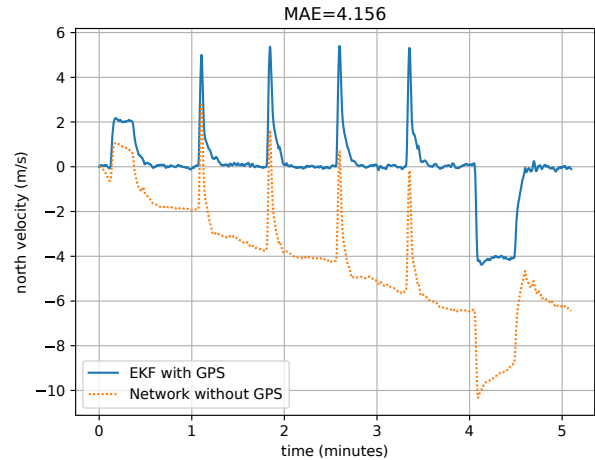


Figure 15: Less attention is paid to velocity errors due to the smaller magnitudes

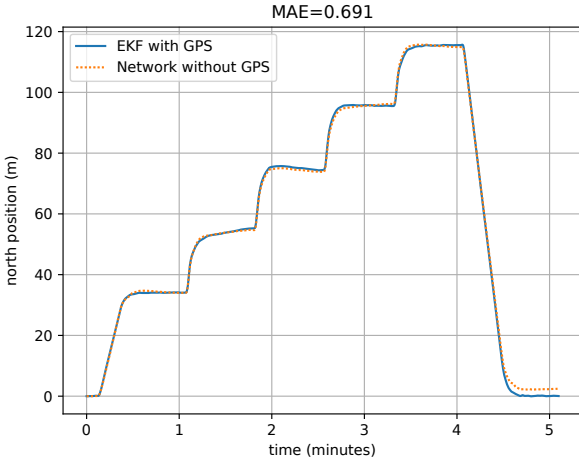


Figure 16: More attention is paid to the large position components, so higher accuracy is achieved

To solve this, a modified MAE was used to account for different signals magnitudes. Equation 1 shows the standard MAE, where \hat{y}_i is the state value predicted by the network, y_i is the true state value, and n is the number of predicted values, $n = 6$ if only velocity and position are required and $n = 10$ if the attitude is required too. Equation 2 is the weighted version, for each signal, the error is multiplied by the signal’s weight so that small errors coming from small signals contribute more fairly to the final loss. The weight for each signal is the reciprocal of its mean in the training set.

$$\text{MAE} = \frac{\sum_{i=1}^n |\hat{y}_i - y_i|}{n} = \frac{\sum_{i=1}^n |e_i|}{n} \quad (1)$$

$$\text{MAE}_{\text{weighted}} = \frac{\sum_{i=1}^n |\hat{y}_i - y_i| w_i}{n} = \frac{\sum_{i=1}^n |e_i| w_i}{n} \quad (2)$$

Using Mean Absolute Percentage Error (MAPE) loss cancels the need for weighting. However, MAPE divides the error by the true value which is often zero. Catching zero divisions and replacing them with machine precision did not solve the problem because the resulting errors were too high. MSE was not better than MAE because most values are small, and squaring made them even smaller resulting in small loss values.

6.2. Network Architecture

Different combinations of dense and recurrent layers were tested, from a single recurrent layer of 10 nodes to 12 layers of 200 nodes each. The best performance was achieved by four recurrent layers, 200 nodes each, followed by a single dense layer of 6 nodes to reshape the data to the shape of the labels (if only velocity and position are required).

6.3. Recurrent Cell Type and Activation Functions

Three different types of recurrent cells were tested; the Vanilla Cell, the Gated Recurrent Unit (GRU), and the Long Short Term Memory (LSTM) cell. Despite taking longer to train and resulting in more parameters, the LSTM cells gave the best performance. Two activations are applied within an LSTM cell, one for the new inputs and another for the recurrent inputs. Sigmoid, tanh and ReLU activations were tested. While tanh had the best performance, it could only be used for input activation. The recurrent activation must be sigmoid for the GPU accelerated training to work.

6.4. Window Size

Window sizes from 20 steps to 200 steps were tested. Increasing the window size increases the accuracy but significantly increases both training and inference time. Too large windows might decrease the accuracy because a larger than needed context leads to network confusion. Table 4 shows the effect of increasing window size on both accuracy and training time.

Table 4: Effect of increasing window size on accuracy and training time

Window size	Median of maximum position errors in validation set (meters)	Training time, 100 epochs (hours)
50	72.4	1.94
100	52.78	4.94
150	35.59	7.25
200	34.26	9.21

6.5. Learning Rate

Learning rates from 0.00001 to 0.1 were tested. In the initial epochs, when the weights are far from their optimal values, high learning rate can be used. When the loss approaches its minimum, the learning rate should be decreased to prevent overshooting. Table 5 was used as a learning rate schedule.

Table 5: Learning rate schedule

Epochs (from - to)	Learning rate
0 - 50	0.005
51 - 100	0.0025
101 - ...	0.001

6.6. Batch Size

The number of training examples (windows) fed to the network in one optimizer step is called batch size. Batching was initially used because GPU memory could not accommodate the entire dataset. Using batches can lead to faster convergence because of the more frequent weights

updates. Batch sizes from 512 to 16,384 windows were tested. The chosen batch size is 1024, as it achieves the fastest learning and provides some regularization.

6.7. Regularization

Regularization is needed to prevent the network from memorizing the training data and allow it to generalize to the validation data. The most popular regularization technique is dropout, which randomly turns off hidden nodes in training time when propagating each input vector. Since two activations are applied, two dropouts are applied, one for the input and another for the recurrent activations. In the earlier trials, dropout gave very good regularization when small number of flight logs was used. Unfortunately, recurrent dropout prevents GPU acceleration, so, it could not be used with large datasets. L1 and L2 regularization were also tested, but they could not achieve similar performance as dropout. The final design and the results shown in this paper do not use any formal regularization.

6.8. Training Time and Number of epochs

An epoch is a single pass through the entire dataset, that is, processing all the batches. Longer training increases training accuracy but may reduce validation accuracy when overfitting occurs. Different numbers of epochs were tested from 100 to 1500, but the accuracy did not increase much after 200 epochs. This takes about 5 hours using two Nvidia RTX 2070 Super GPUs connected via NVLink.

6.9. Final Design

The final network design and hyperparameters used are summarized in Table 6.

Table 6: Network Architecture and Hyperparameters

Number of recurrent layers	4
Number of nodes in a recurrent cell	200
Input activation in recurrent layers	tanh
Recurrent activation in recurrent layers	sigmoid
Number of dense layers	1
Number of nodes in the dense layer	6
Dense activation	None
Optimizer	Adam
Adam’s first & second moment decay rates	0.9, 0.999
Number of Epochs	100 (\approx 5 hours)
Learning rate schedule	0.005, 0.0025, 0.001
Regularization	None
Window size	200 steps = 40 seconds
Batch size	1024 examples
Loss function	Weighted MAE (custom)

7. Results and Discussion

The MPE index defined in section 6 is enough to compare different designs given that the flights in both training and validation sets are unchanged. But when comparing the accuracy of a design in two different flights, MPE alone is not sufficient, because different flights vary in duration and traveled distance. Traditionally, an INS is assessed by the growth of positioning error with time, because the major estimation errors in INS accumulate proportionally to the time since positioning starts. A similar index is used in the following discussions, obtained by dividing the MPE by the flight duration to arrive at Time-Normalized Maximum Position Error (TN-MPE), expressed in meters per minute (m/min).

7.1. Performance on the Training Set

Training performance is usually examined to make sure that the network is at least fitting the training data. No enhancements should be applied to the validation performance until the network sufficiently fits the training data. However, training performance is not a sufficient indicator, and the network must not be expected to provide similar performance on newer data. Training performance might also be treated as a goal to look for in the validation set when tuning the regularization parameters, because it shows the potential of a particular design. Table 7 summarizes the performance on the training set, which consists of 465 flights. The shown median position error indicates that positioning error never grew beyond 7.23 meters in 232 different flights.

Table 7: Performance on the training dataset

	MPE (m)	TN-MPE (m/min)	MVE (m/s)
Mean	16.78	2.98	3.78
Median	7.23	1.39	2.26
Best Flight	1.13	0.45	0.57
Worst Flight	1666.31	262.69	168.02

7.2. Performance on the Validation Set

Validation performance reflects how the system performs with new flights not used during training. The validation dataset is comprised of 83 flights totaling about 8 hours. Table 8 summarizes the performance on the validation set. Mean and median are calculated from the maximum errors reached in every flight. It is noted that the validation mean MPE and TN-MPE are five times larger than those of the training. This resulted from the lack of proper regularization.

Figure 17 shows the flight path of the validation flight with the lowest MPE and TN-MPE. The S letter in a plot indicates the true start position and the E letter indicates the true end position. Some flights seem to start mid-air because the ground time is trimmed as described in section 5.4, and the takeoff portion lies within the first window. As

Table 8: Performance on the validation dataset

	MPE (m)	TN-MPE (m/min)	MVE (m/s)
Mean	85.79	17.79	6.40
Median	34.26	6	4.15
Best Flight	2.66	0.61	0.76
Worst Flight	871.54	142.08	67.65

mentioned in Table 6, the window size is 200 steps. This means that the network makes its first prediction after 40 seconds. By that time, the drone might have already reached the mission altitude.

Despite the path in Figure 17 having some acute direction changes, the network could still predict these maneuvers correctly. One reason is that this flight pattern is common in the dataset, so the network had enough data to relate the associated sensor behavior to the resulting changes in position.

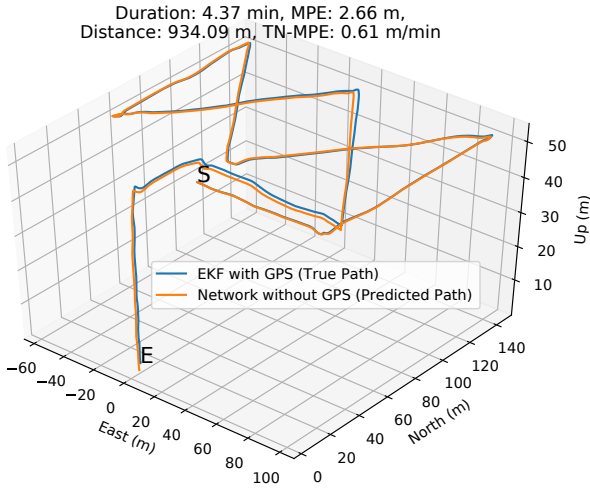


Figure 17: Path of the best validation flight

Figure 18 shows another validation flight with different maneuvers. The blue arrow marks a sudden change in turn rate; an erroneous prediction is made at this point resulting in an offset that persists until the end of the flight.

Figure 19, Figure 20, and Figure 21 show three more validation flights. Despite having the shortest flight duration, the flight in Figure 19 has the highest MPE among the three, and has more than twice as much TN-MPE as any of them. This is because predictions in Figure 19 contain multiple errors near the beginning.

7.3. Aggressive Manual Maneuvers

A common practice in the database flights is that pilots usually start the flight by some aggressive manual maneuvers before switching the autopilot to “Auto” mode that executes the mission autonomously. These aggressive maneuvers might excite some error sources in the IMU that

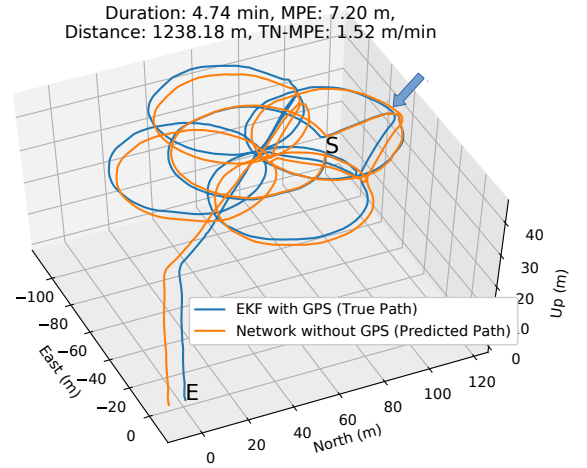


Figure 18: Validation flight path -1

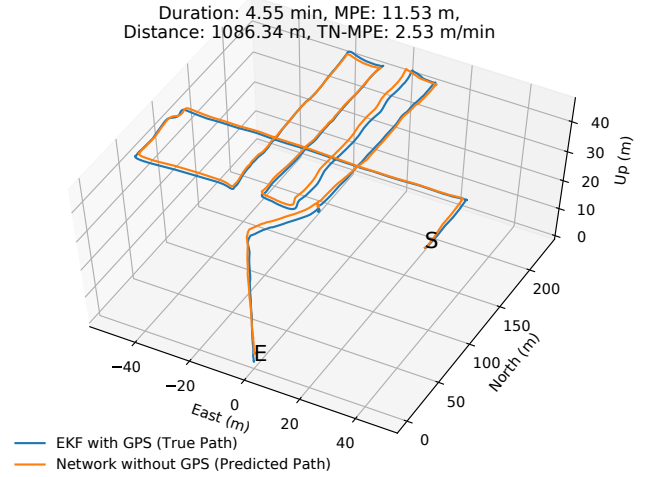


Figure 19: Validation flight path -2

are not active in steady flights. Furthermore, the manual sections of the flights are considerably smaller than the autonomous ones. This, combined with the fact that these maneuvers have much more combinations than the steady ones, means that the data capturing their underlying mappings are *rare* in the dataset. Consequently, the network performance in manual flights is worse than that in autonomous ones. Fortunately, manual flights do not require accurate positioning, and these aggressive maneuvers are usually performed within the pilot’s line of sight. It is the remote autonomous missions and steadier flights that require the proposed system the most.

Figure 22 and Figure 23 show two validation flights with relatively long manual sections. It can be noted that predictions made in these manual sections are worse than those made in the autonomous ones. Despite these erroneous predictions preceding the correct ones, they did not affect them. This means that a single external reset (using an external sensor) can remove much of the error

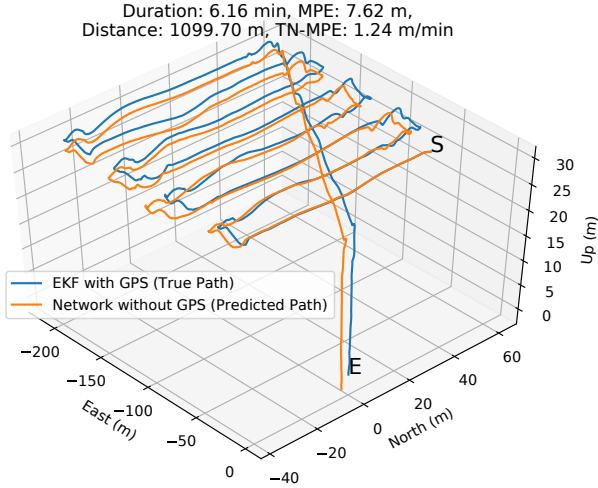


Figure 20: Validation flight path -3

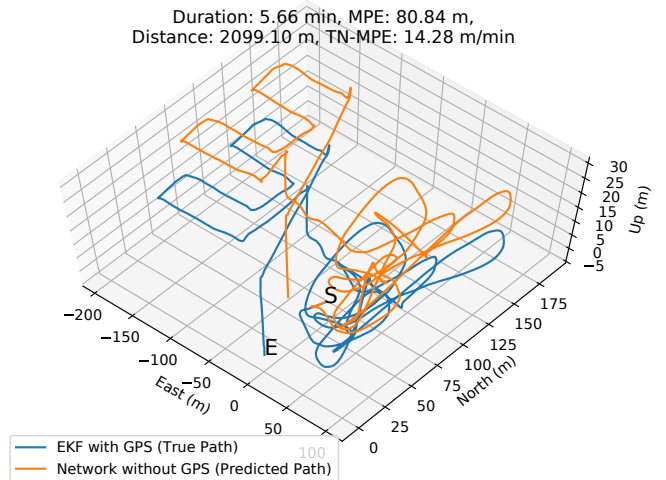


Figure 22: Validation flight with both manual and autonomous sections

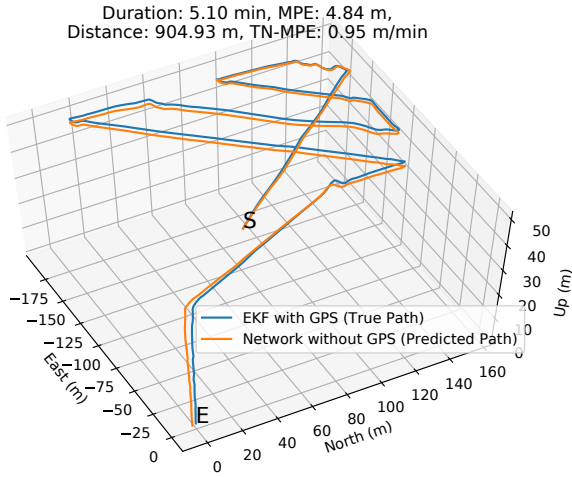


Figure 21: Validation flight path - 4

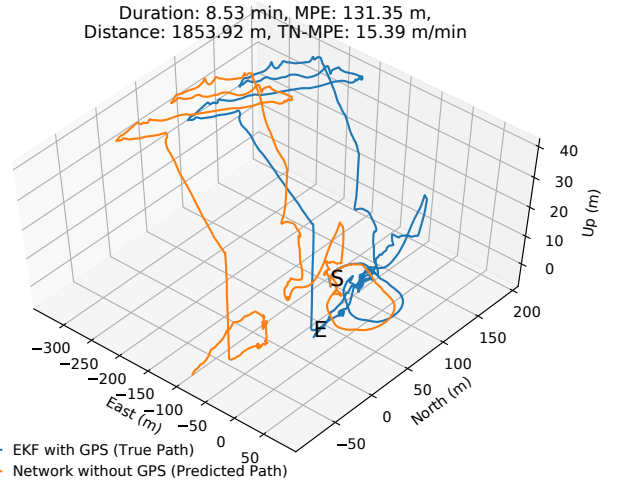


Figure 23: Validation flight with both manual and autonomous sections -2

in the latter segments.

Figure 24 shows another flight where much of the manual maneuvers are hidden in the first window. The ones outside the window were enough to introduce an error that exceeds 120 meters.

The TN-MPE index does not represent the error growth rate, despite having rate units (m/min). This is because much of the prediction errors shown do not grow with time. They are little-varying offsets introduced by rare flight phenomena scattered in different and spaced timesteps. For example, the flight in Figure 24 has a TN-MPE of 28.83 m/min, but this does not mean that if it continued to fly one more minute, the error would have grown by 28.83 meters. Instead, this error was introduced early in the flight and did not change much afterward. This is also visible in Figure 22 and Figure 23, where much of the errors are introduced in the beginning but do not grow later.

7.4. Underrepresented Vehicle Types

It was seen from Table 2 that approximately 94% of the flights in the dataset used a Quadrotor as a host vehicle. The dataset is split randomly into training and validation. Only four flights from the underrepresented vehicles fall into the validation set, of which three used an FW vehicle and one used a VTOL. Performance in these four flights is summarized in Table 9. The TN-MPE Rank column in Table 9 is the position of a flight's TN-MPE among the entire validation set in descending order. It can be seen that these four flights are ranked among the five highest TN-MPEs (lowest accuracy) in the validation set.

Figure 25 shows the FW validation flight # 1. Despite the shorter than a minute duration, positioning error grows beyond a hundred meters. The flight does not have aggressive manual maneuvers either.

The same observation applies to the VTOL validation flight in Figure 26. This, too, is a short flight with smooth

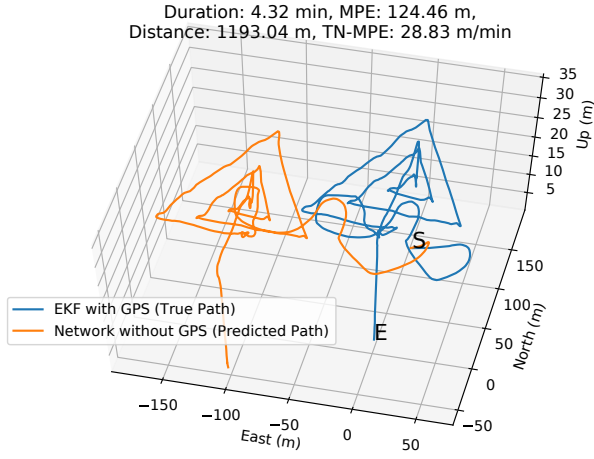


Figure 24: Validation flight with wrong predictions at the beginning

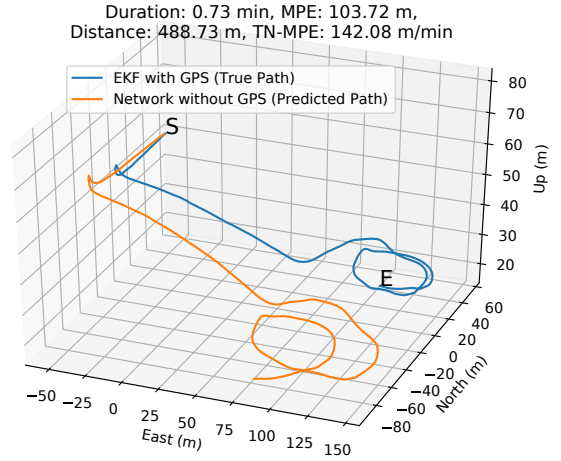


Figure 25: FW Validation Flight # 1

Table 9: Validation performance in underrepresented vehicle types

Flight	Duration (min)	Distance (m)	MPE (m)	TN-MPE (m/min)	TN-MPE Rank
FW #1	0.73	488.73	103.72	142.08	1 st
FW #2	6.52	5424.57	871.54	133.74	2 nd
FW #3	2.6	2062.32	289.82	111.47	4 th
VTOL	5.53	3620.59	551.58	99.8	5 th

maneuvers; still, positioning error grows to almost 300 meters in less than three minutes.

Some factors contributing to the relatively high TN-MPE with underrepresented vehicles are:

1. The network learns to compensate for the Magnetometer errors at some point in the prediction process. These errors are affected mainly by the magnetic field of the vehicle's motors, which varies from one vehicle type to another. For example, an FW drone usually has only one motor, but the Quadrotor has four, and the Standard VTOL has five.
2. The network may be learning to compensate for vibrations, which vary from one vehicle type to another.
3. These flights have relatively high average velocities, the average velocities of the flights in Table 9 range from 10.91 m/s to 13.87 m/s. The mean value of average velocities in the validation set is only 4.66 m/s.

Other than these worst five flights, the sixth-highest TN-MPE in the validation flights is only 52.38 m/min, followed by 38.94 m/min. This explains the large gap between the mean and median values for the TN-MPE in Table 8.

7.5. Velocity Predictions

The network described in Table 6 predicts both position and velocity differences (increments) independently,

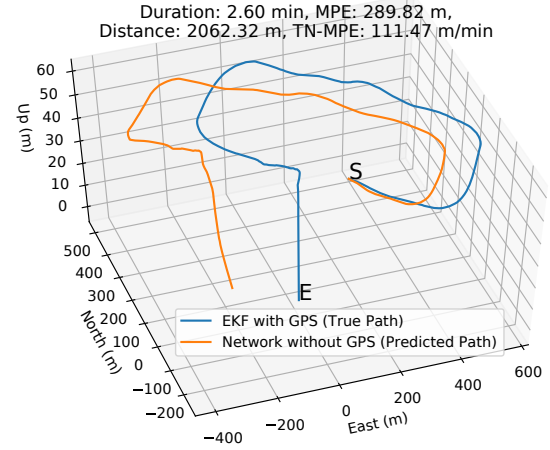


Figure 26: VTOL validation flight

so errors in some direction in velocity are not necessarily reflected in position errors in the same direction. Another method to calculate the velocity is to divide the position differences calculated by the network by the time step. Since the time step is fixed to 0.2 seconds, any predicted position difference can be divided by 0.2 to get the velocity in the same direction. Not only does this reduce the network size and computations, but it also improves the accuracy of the calculated velocity.

Figure 27, Figure 28, and Figure 29 compare the two methods in the three velocity components in a validation flight.

7.6. Attitude Predictions

The PX4 EKF2 estimates the attitude expressed in quaternions. These attitude estimates do not diverge when the GPS signal is lost, because Gyroscope and Accelerometer can predict reliable roll and pitch angles, and the Magnetometer helps correct the yaw angle. Another advantage

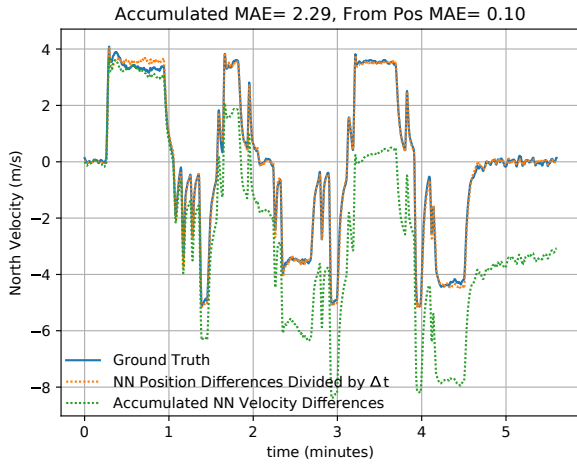


Figure 27: North velocity component of a validation flight as predicted by the network vs. as calculated from position differences

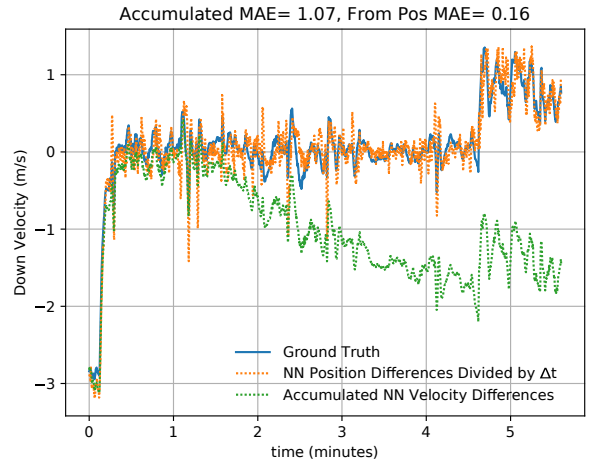


Figure 29: Down velocity component of a validation flight as predicted by the network vs. as calculated from position differences

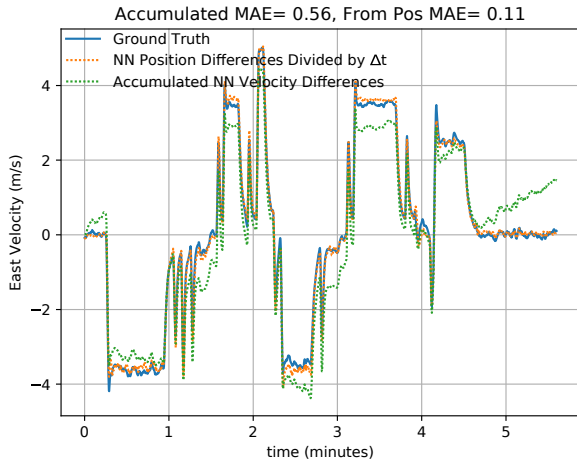


Figure 28: East velocity component of a validation flight as predicted by the network vs. as calculated from position differences

time for both training and inference. Requiring more labels from the network also diverts some focus from the position and velocity calculations and reduces their performance.

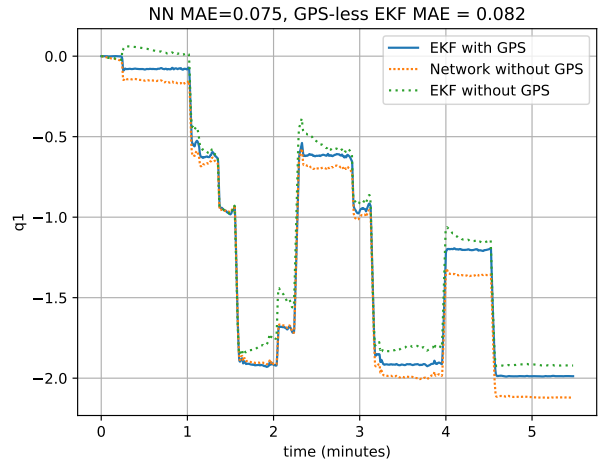


Figure 30: Attitude quaternions - q1

of the EKF's attitude is that it is produced at a relatively high rate of 84 Hz. The network, on the other hand, is trained using 5 Hz logs, so it is limited by this rate. Some trials where the network predicted the attitude along with velocity and position were performed. Figure 30, Figure 31, Figure 32 and Figure 33 show the attitude as predicted by the network and as estimated by the EKF when GPS is lost. The EKF errors here result from the numerical complications caused by the massively diverging position and velocity estimates. In the PX4 code, this is cured by feeding zero position and velocity measurements to the EKF when the GPS fix is lost to preserve the numerical stability of other estimated quantities like the attitude.

These reasonable estimates produced by the GPS-less EKF are the reason why the final network design does not predict attitude. Adding more elements to the labels vector makes the network more complex and requires more

8. Field Testing and Real-time Inference

Inference time is the time taken by the network to predict one labels vector. That is, given a window of sensor measurements, how much time does the network need to predict the corresponding change of position and velocity at the end of this window? Since the network is trained to predict position at 5 Hz, inference time must be less than 200 milliseconds. Inference time is determined by three factors, the embedded hardware on which the network is deployed, the length of the input window, and the size of the network itself. Larger networks achieve higher

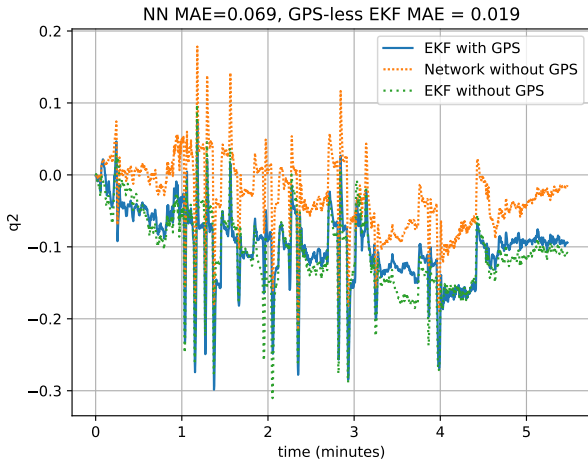


Figure 31: Attitude quaternions - q_2

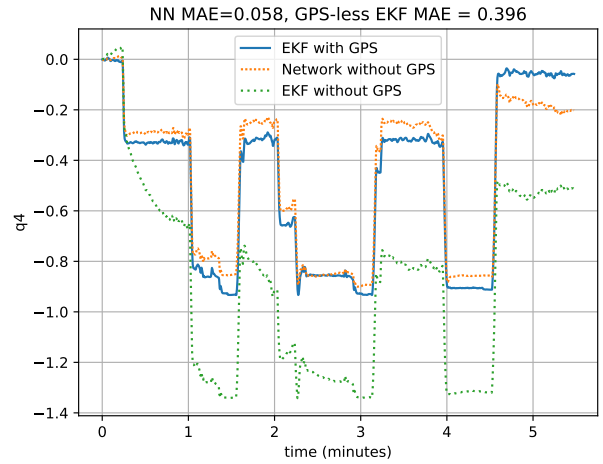


Figure 33: Attitude quaternions - q_4

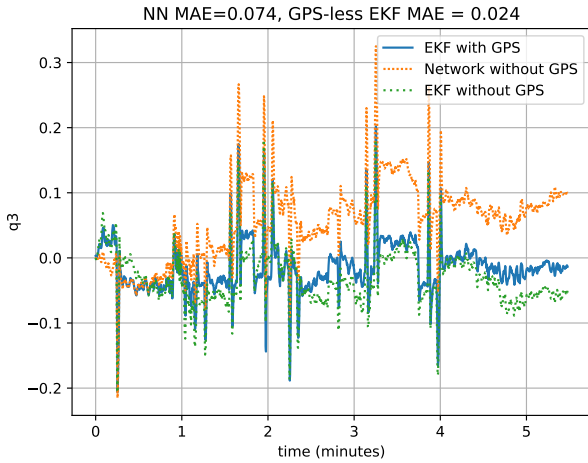


Figure 32: Attitude quaternions - q_3



Figure 34: Companion computers tested to run the network in real-time, from left to right (Raspberry Pi 3 B+, Jetson Nano, Lenovo Laptop)

accuracy but require stronger hardware. Increasing the hardware capabilities comes with increasing size, power consumption, weight, and cost. This is why a compromise is usually made between the network size and its accuracy.

The Pixhawk itself cannot run the heavy NN calculations. This is why a companion computer is usually used alongside it to perform the intensive computations. A smaller version of the network, with only 50 steps window and three labels (position only) was deployed on different companion computers to measure inference time. On a Raspberry Pi 3 B+ [33], inference time is 840 ms, on Nvidia’s Jetson Nano [34], inference time is 200 ms, and on a core i7 laptop [35], inference time is 50 ms. Faster inferences can be achieved with some sacrifice in accuracy. Figure 34 shows the tested companion computers.

To test the real-time performance, a Pixhawk4 was mounted to a car and the laptop running the ground station was also used as the companion computer. The configuration only requires the Pixhawk itself, a GPS receiver

(to compare to ground truth), and a laptop, labeled 1,2 and 3 respectively in Figure 35. The laptop provides power to the Pixhawk, so the battery and power module are not needed. The same cable used to power the Pixhawk from the laptop also works as a data link; this eliminates the need for a telemetry module.

As explained in section 7.4, changing the host vehicle dramatically reduces the network performance. Ground vehicles are not just underrepresented in the training dataset, they are not represented at all. This meant that new logs had to be collected using cars. A total of 34 ground trips were performed using two cars, with a combined duration of about 6.5 hours. Only five trips were held for validation (about half an hour) and the rest were used for training.

A popular technique used in Deep Learning to compensate for the small dataset sizes is Transfer Learning [36, 37]. Transfer learning means that a network trained for some task can be used as a starting point to train another network for another task. For example, the trained weights can be used as the initial weights for a new task,



Figure 35: Hardware Setup in a Car

instead of randomly initializing the weights. This should be done carefully to avoid the loss of the relations learned from the large dataset and at the same time accommodate the new relations introduced by the smaller set.

The same concept can be applied to different vehicle types, for example, a network can be pretrained on Quadrotors, then the knowledge is transferred to a network that works with fixed-wing aircraft, or in this case, a car.

Three experiments were conducted on the light network. The first experiment was to train it on the drones dataset from Table 2 then to use it without any modifications on the cars dataset. The second experiment trains it from scratch on the cars dataset for 100 epochs without utilizing transfer learning. The last experiment is to pretrain it on the drones dataset and then to retrain it on the cars dataset, which is a form of transfer learning. Figure 36 shows the effect of utilizing transfer learning. It is seen that fresh training starts overfitting after 17 epochs, while retraining overfits earlier (around five epochs). This is the point where the network starts to *forget* the relations it has learned from the drones dataset. It is also noticeable that the validation loss is reduced when transfer learning is applied.

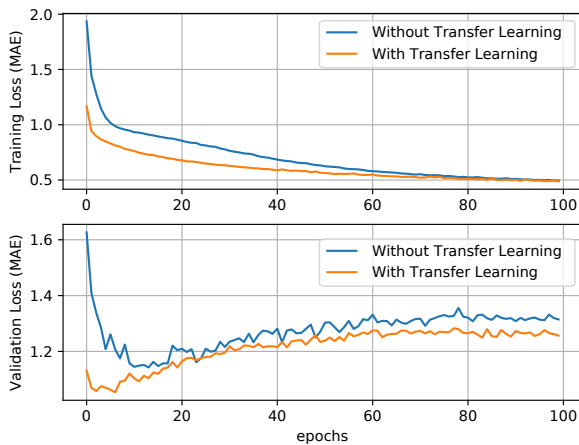


Figure 36: Effect of transfer learning

A comparison between the three experiments is shown in Table 10. The validation results listed utilize early stopping, i.e., overfitting is avoided and the weights used are not the final overfitted weights.

Table 10: Results on the car validation dataset with and without transfer learning

	Trained on drones only	Trained on cars only	Trained on drones, retrained on cars
Median MPE (m)	4250.92	732.12	520.19
Mean MPE (m)	7261.254	1133.324	707.854
Median TN-MPE (m/s)	799.04	99.41	72.99
Mean TN-MPE (m/s)	817.474	181.124	97.222

Table 11 shows the results on the validation car trips obtained when transfer learning is applied.

Table 11: Validation performance on the car dataset

Trip Number	1	2	3	4
Duration (minutes)	5.32	5.58	9.2	11.35
Traveled Distance (Kilometers)	3.314	1.385	8.55	13.79
NN MPE (Kilometers)	0.52	0.136	0.388	1.282
TN-MPE (m/min)	72.99	24.42	56.52	113.05
NN MPE as a Percent of Traveled Distance	11.72 %	9.83 %	6.1 %	9.3 %
GPS-less EKF MPE (Kilometers)	24.184	25.752	203.77	421.99

It is seen from Table 11 that the TN-MPE values of the car trips are lower than those of the FW and VTOL flights mentioned in Table 9. This is because the collected car trips are longer than those of FW and VTOL, and because of the retraining, which gave more attention to this small set.

The accuracy on the car dataset is smaller than that of the flight dataset because the latter is much larger. If higher accuracy is needed on ground vehicles, then more logs must be collected. However, the purpose of car testing in this context is mainly to address the challenges associated with real-time inference (edge computing).

Several complications arise when edge computing is performed. Aside from accuracy loss resulting from the inevitable network size reduction, other issues like timing, proper preprocessing, data validity, and latency also affect the NN predictions. Most of these complications affect the features consumed by the network. For example, the network makes a prediction every 200 milliseconds; timing this loop on a full operating system -rather than a real-time OS- is hard to guarantee. Consequently, a ± 1 ms timing error is introduced, this affects both averaging and differencing steps in preprocessing. Furthermore,

since sensors operate at different rates, multi-threading is needed to capture every sensor’s measurements as soon as they are published. And to avoid data loss, these measurements should be stored in queues before they are fed to the NN. But if these queues are allowed to grow indefinitely, then latency in NN predictions will be noticed, so a compromise should be made. Another issue is data validity; having different functions writing to the features array can easily result in data corruption due to race conditions. After addressing all these issues, the NN predictions made in real-time are compared to those made offline using the logged data. Figure 37, Figure 38 and Figure 39 show the online and offline position predictions made on a validation trip.

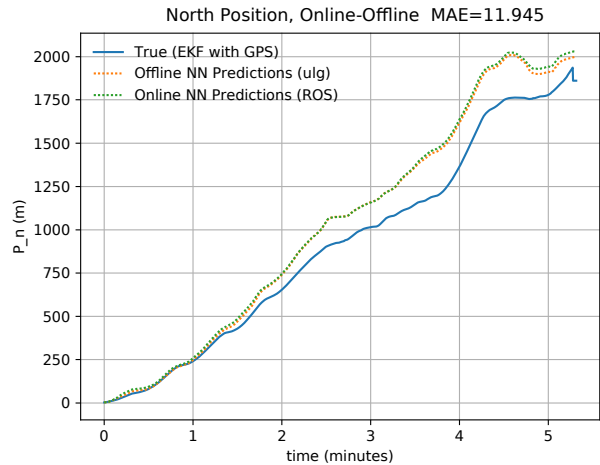


Figure 39: Validation ground trip, online vs. offline predictions, down position

9. Summary and Conclusion

The paper presented a Neural Network capable of predicting a drone’s 3D position and speed in the absence of GPS using the IMU, Barometer and Magnetometer raw measurements. The developed network was tested on several hardware targets, and can run with acceptable speed on embedded devices like the Jetson Nano. Errors in 3D position as low as 2.7 were achieved using the proposed system in 5-minutes GPS-less drone flight using low-cost sensors. The system is well integrated with the PX4 flight stack running on Pixhawk4 and can be used with a quick setup. The system can also predict the attitude, but the EKF is more reliable in such a task. The network is designed to make inferences at 5 Hz, so it is slower than the EKF. This is why the network’s main role is to replace the GPS, not the entire EKF. The network is ideally used with Quadrotors running on “Auto” flight mode because most of the training data have these characteristics. Transfer learning is also used, and the system was tested in real-time with a ground host vehicle. The network’s errors associated with manual maneuvers or less popular host vehicles can be reduced by collecting more training data focusing on these conditions. Navigation accuracy also increases when a larger network and window size are used. But this comes at the expense of both training and inference times. The median positioning error on the validation set is five times larger than that of the training set. This signals the need for proper regularization to help the network generalize better.

References

- [1] M. Bloesch, S. Omari, M. Hutter, R. Siegwart, Robust visual inertial odometry using a direct EKF-based approach, in: 2015 IEEE/RSJ International Conference on Intelligent Robots and Systems (IROS), IEEE, 2015. doi:10.1109/iros.2015.7353389.

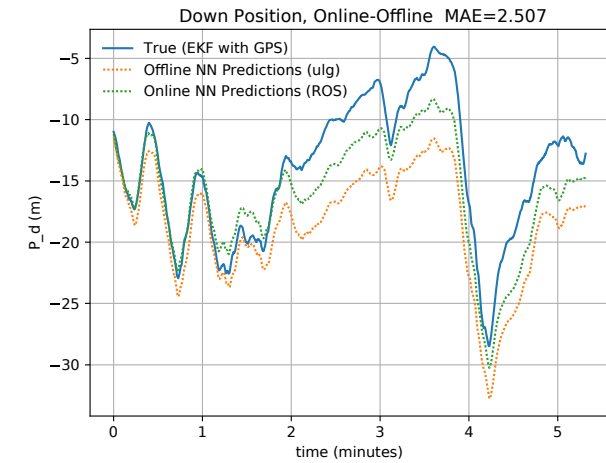


Figure 37: Validation ground trip, online vs. offline predictions, north position

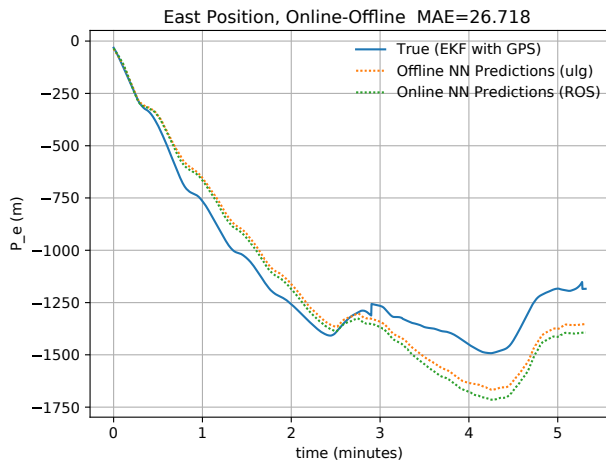


Figure 38: Validation ground trip, online vs. offline predictions, east position

- [2] K. Chiang, G. Tsai, H. Chang, C. Joly, N. El-Sheimy, Seamless navigation and mapping using an INS/GNSS/grid-based SLAM semi-tightly coupled integration scheme, *Information Fusion* 50 (2019) 181–196. doi:10.1016/j.inffus.2019.01.004.
- [3] T.-D. Vu, J. Burlet, O. Aycard, Grid-based localization and local mapping with moving object detection and tracking, *Information Fusion* 12 (1) (2011) 58–69. doi:10.1016/j.inffus.2010.01.004.
- [4] E. Choi, S. Chang, A consumer tracking estimator for vehicles in GPS-free environments, *IEEE Transactions on Consumer Electronics* 63 (4) (2017) 450–458. doi:10.1109/tce.2017.015064.
- [5] J. W. David Titterton, *Strapdown Inertial Navigation Technology*, Institute of Electrical Engineers, 2009. URL https://www.ebook.de/de/product/21923218/david_titterton_john_weston_strapdown_inertial_navigation_technology.html
- [6] K.-W. Chiang, A. Noureldin, N. El-Sheimy, Multisensor integration using neuron computing for land-vehicle navigation, *GPS Solutions* 6 (4) (2003) 209–218. doi:10.1007/s10291-002-0024-4.
- [7] K.-W. Chiang, H.-W. Chang, C.-Y. Li, Y.-W. Huang, An artificial neural network embedded position and orientation determination algorithm for low cost MEMS INS/GPS integrated sensors, *Sensors* 9 (4) (2009) 2586–2610. doi:10.3390/s90402586.
- [8] L. Semenik, A. Noureldin, Bridging GPS outages using neural network estimates of INS position and velocity errors, *Measurement Science and Technology* 17 (10) (2006) 2783–2798. doi:10.1088/0957-0233/17/10/033.
- [9] C. Shen, Y. Zhang, J. Tang, H. Cao, J. Liu, Dual-optimization for a MEMS-INS/GPS system during GPS outages based on the cubature kalman filter and neural networks, *Mechanical Systems and Signal Processing* 133 (2019) 106222. doi:10.1016/j.ymsp.2019.07.003.
- [10] Z. Wu, W. Wang, INS/magnetometer integrated positioning based on neural network for bridging long-time GPS outages, *GPS Solutions* 23 (3) (jun 2019). doi:10.1007/s10291-019-0877-4.
- [11] N. El-Sheimy, K.-W. Chiang, A. Noureldin, The utilization of artificial neural networks for multisensor system integration in navigation and positioning instruments, *IEEE Transactions on Instrumentation and Measurement* 55 (5) (2006) 1606–1615. doi:10.1109/tim.2006.881033.
- [12] J. J. Wang, J. Wang, D. Sinclair, L. Watts, A neural network and kalman filter hybrid approach for gps/ins integration, in: *Proceedings of the Korean Institute of Navigation and Port Research Conference*, Vol. 1, Korean Institute of Navigation and Port Research, 2006, pp. 277–282.
- [13] Y. Yao, X. Xu, C. Zhu, C.-Y. Chan, A hybrid fusion algorithm for GPS/INS integration during GPS outages, *Measurement* 103 (2017) 42–51. doi:10.1016/j.measurement.2017.01.053.
- [14] H. fa Dai, H. wei Bian, R. ying Wang, H. Ma, An INS/GNSS integrated navigation in GNSS denied environment using recurrent neural network, *Defence Technology* 16 (2) (2020) 334–340. doi:10.1016/j.dt.2019.08.011.
- [15] C. Shen, Y. Zhang, X. Guo, X. Chen, H. Cao, J. Tang, J. Li, J. Liu, Seamless GPS/inertial navigation system based on self-learning square-root cubature kalman filter, *IEEE Transactions on Industrial Electronics* 68 (1) (2021) 499–508. doi:10.1109/tie.2020.2967671.
- [16] A. Noureldin, A. El-Shafie, M. Bayoumi, GPS/INS integration utilizing dynamic neural networks for vehicular navigation, *Information Fusion* 12 (1) (2011) 48–57. doi:10.1016/j.inffus.2010.01.003.
- [17] J. Li, N. Song, G. Yang, M. Li, Q. Cai, Improving positioning accuracy of vehicular navigation system during GPS outages utilizing ensemble learning algorithm, *Information Fusion* 35 (2017) 1–10. doi:10.1016/j.inffus.2016.08.001.
- [18] X. Li, W. Chen, C. Chan, B. Li, X. Song, Multi-sensor fusion methodology for enhanced land vehicle positioning, *Information Fusion* 46 (2019) 51–62. doi:10.1016/j.inffus.2018.04.006.
- [19] Y. Bai, B. Zhang, S. Chai, X. Jin, X. Wang, T. Su, Continuous estimation of motion state in GPS/INS integration based on NARX neural network, in: *2018 37th Chinese Control Conference (CCC)*, IEEE, 2018. doi:10.23919/chicc.2018.8483157.
- [20] V. Havyarimana, D. Hanyurwimfura, P. Nsengiyumva, Z. Xiao, A novel hybrid approach based-SRG model for vehicle position prediction in multi-GPS outage conditions, *Information Fusion* 41 (2018) 1–8. doi:10.1016/j.inffus.2017.07.002.
- [21] L. Meier, P. Tanskanen, F. Fraundorfer, M. Pollefeys, PIX-HAWK: A system for autonomous flight using onboard computer vision, in: *2011 IEEE International Conference on Robotics and Automation*, IEEE, 2011. doi:10.1109/icra.2011.5980229.
- [22] L. Meier, D. Honegger, M. Pollefeys, PX4: A node-based multithreaded open source robotics framework for deeply embedded platforms, in: *2015 IEEE International Conference on Robotics and Automation (ICRA)*, IEEE, 2015. doi:10.1109/icra.2015.7140074.
- [23] J. García, J. M. Molina, J. Trincado, Real evaluation for designing sensor fusion in UAV platforms, *Information Fusion* 63 (2020) 136–152. doi:10.1016/j.inffus.2020.06.003.
- [24] P. Riseborough, R. Bapst, L. Meier, C. Olsson, Siddharth Bharat Purohit, M. Sauder, J. Oes, Georgehines, B. Tak, D. Agar, W. Johnson, M. Charlebois, Nickolasrossi, Pickledgator, B. Küng, Ecl: V0.9.0 release (2016). doi:10.5281/ZENODO.55367.
- [25] PX4.Community, *Px4 flight logs database*. URL <https://review.px4.io/browse>
- [26] H. Willee, P. Fjare, *Pixhawk 4 flight controller*. URL https://docs.px4.io/v1.9.0/en/flight_controller/pixhawk4.html
- [27] Invensense, *High performance 6-axis mems motiontracking device in 4x4 mm package*. URL <https://invensense.tdk.com/wp-content/uploads/2017/08/ICM-20689-v2.2-002.pdf>
- [28] B. Sensortec, *Bmi055 small, versatile 6dof sensor module*. URL <https://www.bosch-sensortec.com/media/boschsensortec/downloads/datasheets/bst-bmi055-ds000.pdf>
- [29] Isentek, *Ist8310 3d magnetometer brief datasheet*. URL [http://www.isentek.com/en/dlf.php?file=../ISENTEK/\(201703-09\)IST8310Datashetv1.2-brief-105.09.20.pdf](http://www.isentek.com/en/dlf.php?file=../ISENTEK/(201703-09)IST8310Datashetv1.2-brief-105.09.20.pdf)
- [30] TE, *Ms5611-01ba03 barometric pressure sensor, with stainless steel cap*. URL https://www.te.com/commerce/DocumentDelivery/DDEController?Action=showdoc&DocId=DataSheetMS5611-01BA03B3pdfEnglishENG_DS_MS5611-01BA03_B3.pdfCAT=BLPS0036
- [31] J. T. Jang, A. Santamaria-Navarro, B. T. Lopez, A. akbar Agha-mohammadi, Analysis of state estimation drift on a MAV using PX4 autopilot and MEMS IMU during dead-reckoning, in: *2020 IEEE Aerospace Conference*, IEEE, 2020. doi:10.1109/aero47225.2020.9172736.
- [32] M. S. Grewal, A. P. Andrews, C. G. Bartone, *Global Navigation Satellite Systems, Inertial Navigation, and Integration*, John Wiley and Sons Ltd, 2020.
- [33] R. P. FOUNDATION, *Raspberry pi 3 model b+*. URL <https://www.raspberrypi.org/products/raspberry-pi-3-model-b-plus/>
- [34] NVIDIA, *Nvidia jetson nano datasheet*. URL <https://developer.nvidia.com/embedded/dlc/jetson-nano-system-module-datasheet>
- [35] Lenovo, *Lenovo z510 laptop*. URL <https://www.lenovo.com/us/en/laptops/lenovo/z-series/z510/>
- [36] C. Tan, F. Sun, T. Kong, W. Zhang, C. Yang, C. Liu, A survey on deep transfer learning [arXiv:1808.01974v1](https://arxiv.org/abs/1808.01974v1).
- [37] K. Weiss, T. M. Khoshgoftaar, D. Wang, A survey of transfer learning, *Journal of Big Data* 3 (1) (may 2016). doi:10.1186/s40537-016-0043-6.